Electrochemical Pd Nanodeposits on a Au Nanoisland Template Supported on Si(100): Formation of Pd–Au Alloy and Interfacial Electronic Structures

Youngku Sohn,[†] Debabrata Pradhan, and K. T. Leung*

WATLab and Department of Chemistry; University of Waterloo, Waterloo, Ontario N2L 3G1 Canada. [†]Present address: Department of Chemistry, Yeungnam University, Gyeongsan, Gyeongbuk 712-749, South Korea.

Transition metals have played an extremely important role in many technological areas including chemical industry, automobiles and green energy production, often used as catalysts in promoting specific reactions.[1–8] Palladium is one of the most active transition metals that have been widely used for efficient chemical conversion, especially as a catalyst for complete CO oxidation of automobile exhaust in a catalytic converter.[6,7] Pd-based materials have also been used as important industrial catalysts for the synthesis of vinyl acetate from ethylene, acetic acid, and oxygen.[1,8–10] In recent years, much research has been devoted to improving the catalytic activity and selectivity of Pd, for example, by adding Au[7–10] and other metals,[11,12] and to understanding the reaction mechanisms of specific reactions. In particular, Chen et al. demonstrated that a low coverage of Pd on Au could significantly enhance acetoxylation of ethylene in the production of vinyl acetate.[8] The enhanced activity has been explained by geometrical and/or electronic effects,[8–10,13] with the relative Pd–to–Au composition being another very important factor. Furthermore, the Pd–Au catalyst has been demonstrated to be very efficient and selective for direct hydrogen peroxide synthesis from H_2/O_2 mixtures at low temperature.[14–16] The H_2O_2 synthesized by this method could be regarded as a promising environmentally green oxidant.[16] Moreover, Enache et al. demonstrated that oxidation of primary alcohols to aldehydes could be greatly enhanced on Au-rich and Pd-rich core–shell PdAu nanoparticles (NPs) supported on TiO_2.[4] Scott et al. reported that for

ABSTRACT Palladium nanoparticles have uniformly been electrodeposited on a Au nanoisland template (NIT) supported on a Si(100) substrate, which exhibits Au-rich, Pd-rich, and/or polycrystalline mixed structures upon annealing to 700 °C. Glancing-incidence X-ray diffraction (GIXRD) and energy-dispersive X-ray (EDX) elemental analysis of the as-deposited sample both show metallic Pd, while depth-profiling X-ray photoelectron spectroscopy (XPS) further reveals the presence of Pd–Au (and Pd_xSi) at the interfaces of the Pd nanodeposits on the Au NIT. Upon the sample being annealed to 700 °C, both Pd $3d_{3/2}$ and Au $4f_{7/2}$ XPS peaks are found to shift to lower binding energies, which further confirms Pd–Au alloy formation. The convergence of respective GIXRD features of metallic Au and Pd toward intermediate peak positions supports the formation of alloy and their crystalline nature. Depth-profiling XPS analysis of the annealed sample further shows that the Pd nanoparticles are found to consist of an ultrathin shell of PdO_2, and a PdO-rich (i.e., Pd-poor) inner-core, which is consistent with the observed GIXRD patterns of PdO and Pd–Au alloy but indiscernible PdO_2. We compare the above results with the experimental results for electrodeposited Pd on a bare Si(100) substrate. Our study provides new insight into the formation of Pd–Au alloy composite on Si by electrochemistry. The easy control of the Pd, Au, and Pd–Au composition in the nanodeposits as illustrated in the present method offers new flexibility for developing hybrid nanocatalysts and other applications.

KEYWORDS: Pd nanoparticle · Au nanoparticle template · Pd–Au alloy nanostructure · interfacial electronic structures · selective electrodeposition · X-ray diffraction · X-ray photoelectron spectroscopy

CO oxidation the catalytic activity of TiO_2-supported PdAu bimetallic NPs was enhanced relative to that of Pd-only or Au-only catalysts.[7] The PdAu bimetallic catalyst is also known to be very efficient for coupling and cyclization of acetylene to selectively form benzene.[17,18] Some other chemical reactions exhibiting enhanced efficiencies when PdAu catalysts were used include selective hydrogenation of 1,3-butadiene[19] and glycerol oxidation.[20] These studies also show that the efficiency and selectivity strongly depend on the relative composition of Pd and Au in the PdAu catalysts.[19–21]
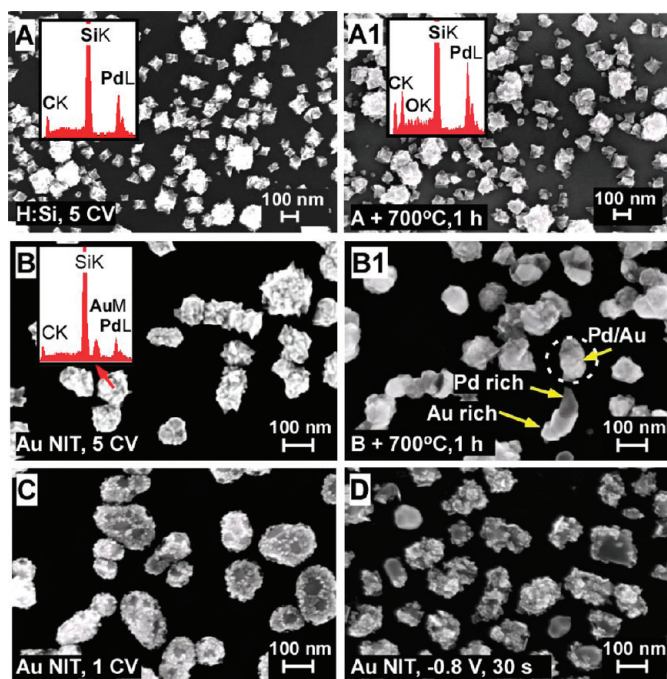
These studies have illustrated great opportunities in developing new applications

Figure 1. SEM images and EDX spectra (insets) for Pd nanoparticles electrodeposited on (A) a H-terminated Si(100) substrate, and (B) a Au nanoisoland template (NIT) prepared by five cycles of cyclic voltametry (CV) from 0.0 to +0.5 to 0.0 V, and after annealing the respective samples to 700 °C for 1 h (A1 and B1), as well as on a Au NIT obtained by (C) one CV cycle and (D) amperometry at −0.8 V for 30 s.

by varying the nature of this type of PdAu bimetallic systems and have motivated us to investigate the PdAu bimetallic system in more detail. Bimetallic Pd/Au or Au/Pd materials in the forms of films, and NPs with hybrid (alloy) or core−shell structures have been prepared by thermal evaporation of one metal onto the other metal, solution chemistry involving mixed solutions, or stepwise addition and treatment of solutions.[7,22−27] Electrodeposition of Pd on bulk Au substrates (including codeposition of Pd and Au ions[28]) have also been reported.[29−32] In the present work, we first prepare a Au nanoisland template (NIT) on a Si(100) substrate, with near-regularly spaced Au nanoislands, by sputter-deposition followed by thermal annealing. We then electrochemically deposit Pd NPs onto the Au NIT to produce the Pd−Au nanostructures. Using this procedure, Pd can be "selectively" electrodeposited only on the Au nanoislands and not on the nonconducting thermal oxide areas between the Au nanoislands on the Si(100) support. This approach offers a unique core−shell bimetallic Pd−Au nanostructured, templated system with easily controllable average size distributions, number densities and pitch spacings (among the nanoislands), appropriate for nanocatalysis and other applications. The morphology and crystal structure, as well as the chemical-state composition and interfacial electronic structure are studied in detail by using scanning electron microscopy (SEM), glancing-incidence X-ray diffraction (GIXRD), and depth-profiling X-ray photoelectron spectroscopy (XPS).

RESULTS AND DISCUSSION

Growth Morphology of Pd NPs on Supported Au NIT. Figure 1 shows the SEM images of electrodeposited Pd on hydrogen-terminated Si(100) (H:Si) and on Au NIT prepared under various experimental conditions, including (sample A) Pd NPs electrodeposited on H:Si prepared by five cycles of cyclic voltametry (CV) (Supporting Information, Figure S1); (sample B) Pd NPs electrodeposited on a Au NIT by 5 CV cycles; (sample C) Pd NPs electrodeposited on a Au NIT by 1 CV cycle; and (sample D) Pd NPs deposited on a Au NIT by amperometry potentiostatically at −0.8 V for 30 s. All CV cycles were performed by scanning from 0.0 to +0.5 V in the positive (forward) direction and then in the negative (reverse) direction at a scan rate of 0.01 V s^{-1}. Samples A1 and B1 correspond to, respectively, samples A and B upon annealing at 700 °C for 1 h. The corresponding energy-dispersive X-ray analysis (EDX) data for samples A, A1, and B are also shown as insets in Figure 1. For the Pd NPs on the H:Si (sample A) and Au NIT supports (sample B), the respective EDX spectra reveal that, in addition to the intense Si substrate features, C and Pd features are clearly present without any discernible O feature. This indicates that the as-electrodeposited Pd is zero-valent metallic without any discernible Pd oxides or thick Si thermal oxides on both the H:Si and Au NIT supports. For the annealed sample A1, however, the corresponding EDX spectrum clearly exhibits a prominent oxygen peak, which indicates the presence of PdO$_x$ (x = 1, 2) as confirmed by the corresponding XPS and XRD data shown below. Upon being annealed to 700 °C, the surface morphology of sample B1 dramatically changes to grain structures with the SEM images showing brighter and darker regions for Au-rich and Pd-rich areas, respectively. In addition, the thickness of the silicon oxide layer (for both samples A1 and B1) has been dramatically increased (Supporting Information, Figure S2). After conducting EDX analysis at different spots of selected NPs, we identify three general types of distinct areas: (a) a Pd/Au area with comparable Pd L and Au M line intensities, (b) a brighter Au-rich area with the Au intensity greater than the Pd intensity, and (c) a darker Pd-rich area with the Au intensity smaller than the Pd intensity. These three areas (Supporting Information, Figure S3) also exhibit O signals comparable to the Pd intensities due to oxidation of Pd during annealing in air. For sample C, the Pd NPs deposited on a Au NIT by 1 CV cycle appear to be distributed more uniformly than those deposited by amperometry at −0.8 V for 30 s (sample D).

Figure 2 shows the corresponding magnified SEM images for samples A, B, C, and D, depicting the progressive growth evolution of Pd NPs on the H:Si and Au NIT substrates electrodeposited by both CV and amperometry. Evidently, jagged cuboid Pd NPs with a wide range of sizes from less than 10 nm to over 200 nm are found on the H:Si substrate (Figure 2a). On the other hand, smaller Pd NPs are progressively deposited on the Au NIT apparently in a mixed 2D layer and 3D island

growth (Stranski−Krastanov) mode, initially as small (<10 nm) NPs partially covering the Au nanoislands after 1 CV cycle and then as larger jagged cuboid NPs (resembling those found on H:Si) completely covering the Au nanoislands after 5 CV cycles (Figure 2b). Similar growth evolution is also observed for Pd deposited on a Au NIT by amperometry, first as NP patches partially covering the Au nanoislands at −0.8 V for 30 s and becoming larger layered NPs that cover the entire Au nanoislands at a more negative voltage of −1.0 V for 20 s (Figure 2c). It is clear that the Pd NPs are stacking on top of other NPs with no apparent ordering as the deposition continues.
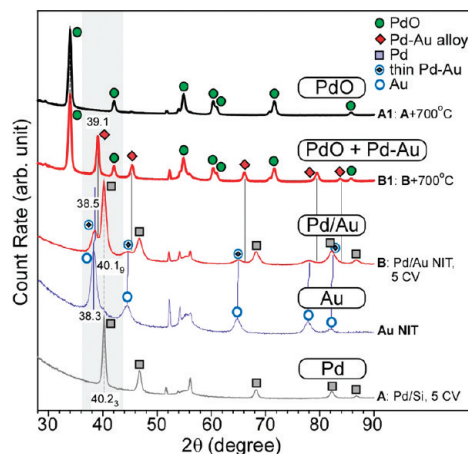
Figure 3 compares the GIXRD patterns of Pd NPs electrodeposited on H:Si (sample A), and on Au NIT (sample B) before and after annealing at 700 °C for 1 h (samples A1 and B1). The XRD pattern of the Au NIT (also shown in Figure 3) is in good agreement with the fcc metallic Au reference (JCPDS 65-2870).[33] For the as-deposited Pd NPs on H:Si (sample A), the corresponding XRD pattern is in good accord with that of the fcc ($Fm\bar{3}m$) structure of metallic Pd (JCPDS 01-087-0639),[34] with no detectable features attributable to Pd oxides consistent with the EDX result (Figure 1A, inset). Upon sample A being annealed to 700 °C, the resulting sample A1 exhibits a markedly different XRD pattern that is characteristic of tetragonal ($P42/mmc$) PdO structure (JCPDS 00-041-1107).[34] For the Pd NPs as-deposited on Au NIT (sample B), the corresponding XRD pattern contains the XRD patterns of both metallic Pd and Au. Upon careful examination of the selected shaded region near $2\theta = 40°$, we found that the Au(111) peak at 38.3° of Au NIT is shifted to 38.5° in sample B by +0.2°, while the Pd(111) peak at $40.2_3°$ of Pd is shifted to $40.1_9°$ by $-0.0_4°$ in sample B. Although these shifts appear to be rather small, they suggest the formation of PdAu alloy, as discussed further below in our XPS data. The XRD shift for Pd is found to be within the instrumental resolution (0.04°) while that for Au is discernibly larger. These shifts suggest that there are more structural changes to Au than to Pd in the formation of the alloy nanostructure. More dramatic changes can be found in the XRD pattern of sample B1, obtained upon annealing sample B to 700 °C. In particular, the corresponding XRD pattern contains that of PdO and a set of peaks that clearly lie in between those of metallic Pd and Au. For example, the new peak at 39.1° in the shaded region is located +0.8° from the Au(111) feature at 38.3° in the Au NIT and $-1.0_9°$ from the Pd(111) feature at $40.1_9°$ in sample B. We attribute the observed new set of "in-between" peaks at 39.1°, 45.4°, 66.1°, 79.5°, and 83.8° (marked by solid diamonds) to the formation of PdAu alloy (obtained upon annealing the Pd NPs on Au NIT to 700 °C), consistent with that reported in the literature.[35]

Depth-Profiling XPS Studies of Pd NPs Supported on H:Si and on Au NIT. Figure 4 shows the XPS spectra of the Pd 3p, Pd 3d, O 1s and valence band (VB) regions of Pd NPs as-deposited on H:Si(100) (sample A, upper panel) and
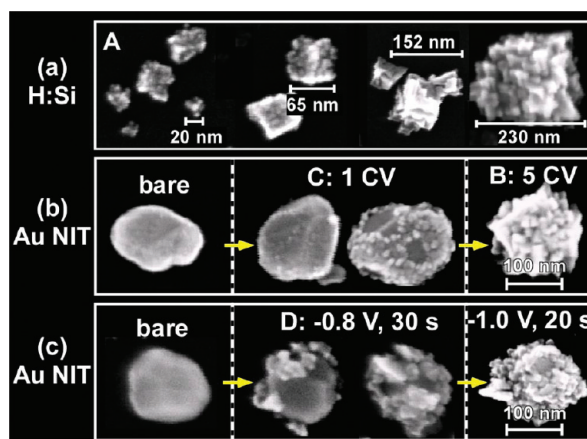
Figure 2. Magnified SEM images depicting the progressive mixed 2D layer and 3D island growth modes of Pd nanodeposits on H:Si for (a) sample A, on a Au nanoisland template (NIT) for (b) samples B and C by cyclic voltametry (CV), and for (c) sample D and another sample obtained at −0.8 V for 30 s and −1.0 V for 20 s, respectively, by amperometry.

after annealing to 700 °C for 1 h (sample A1, lower panel). For the as-deposited sample A (Figure 4, upper center), the Pd $3d_{5/2}$ (Pd $3d_{3/2}$) peak at 335.2 eV (340.5 eV) binding energy (BE), with a measured spin−orbit splitting of 5.3 ± 0.1 eV, is found to be in good accord with those of metallic Pd.[36,37] No Pd $3d_{5/2}$ features attributable to PdO (expected at 336−337 eV) and PdO$_2$ (at ∼338 eV) are observed, which indicates that the surface of the Pd nanodeposit is mainly metallic Pd without any discernible oxide overlayer, in good accord with the lack of O related features in the corresponding EDX (Figure 1) and XRD data (Figure 3). Upon 15 s sputtering, the Pd $3d_{5/2}$ ($3d_{3/2}$) peak is found to shift to 335.5 eV (340.8 eV) by +0.3 eV (to a higher BE) with its intensity increased considerably and spectral profile becoming sharper and symmetric (Supporting Information, Figure S4). The intensity enhancement is likely due to the removal of a carbonaceous layer (commonly found due to

Figure 3. Glancing incidence XRD patterns for a Au nanoisland template (NIT), and Pd nanoparticles electrodeposited on H:Si (sample A) and on a Au NIT (sample B) by 5 cyclic voltametry (CV) cycles, and after annealing the respective samples to 700 °C for 1 h (samples A1 and B1). The PdAu alloy features are marked by solid diamonds.
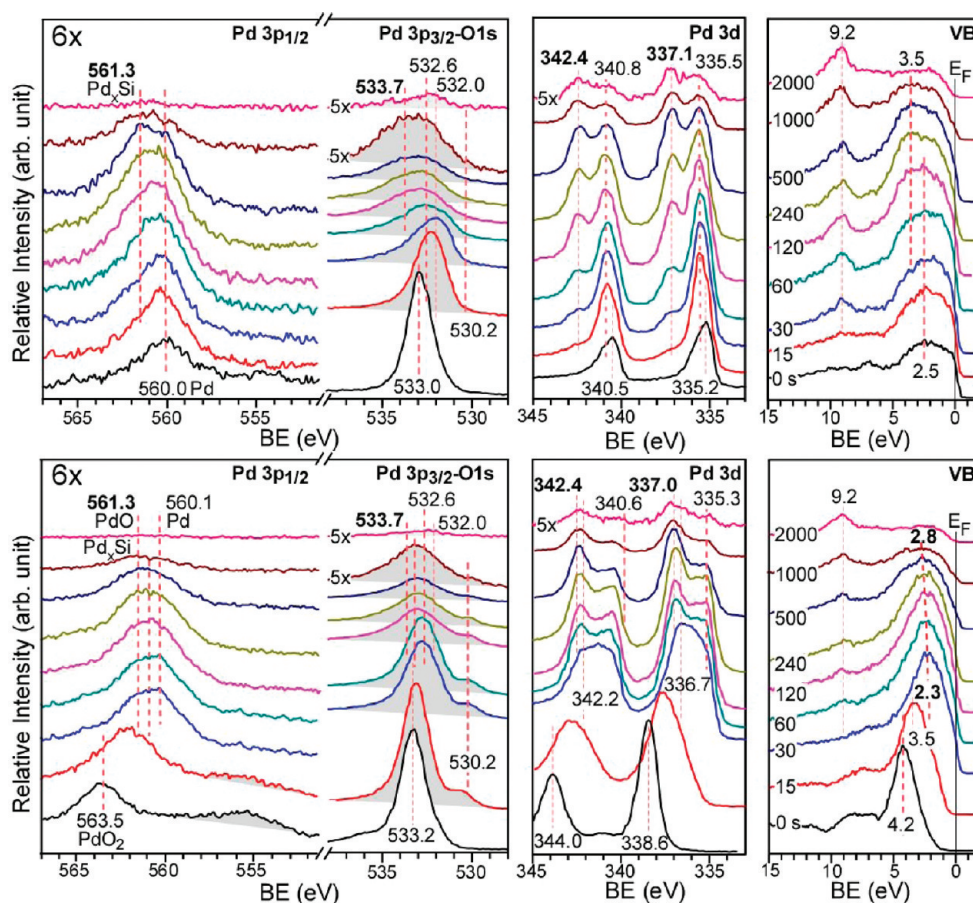
Figure 4. XPS spectra of the Pd 3p and O 1s (left), Pd 3d (center), and valence band (VB) regions (right) for Pd NPs as-electrodeposited on H:Si(100) (sample A, upper) and after annealing at 700 °C for 1 h (sample A1, lower), and upon sputtering for 15, 30, 60, 120, 240, 500, 1000, and 2000 s.

sample handling in air) by the initial sputtering. Located at 1.6 eV higher BE than the metallic Pd, a new Pd $3d_{5/2}$ (Pd $3d_{3/2}$) feature at 337.1 eV (342.4 eV), first appearing as a weak shoulder after 15 s of sputtering, is found to grow to considerable intensity that is comparable to that of the metallic feature after 500 s of sputtering. This new feature could be assigned to Pd silicide and/or PdO, both of which exhibit a similar BE position.[36,37] The formation of Pd silicide (Pd_xSi) has been reported for thermally evaporated Pd on a Si surface,[38–42] while the interfacial electronic structure of electrodeposited Pd on Si has not been reported. For a pristine thermally evaporated Pd on Si, Dai and Davoli observed a Pd $3d_{5/2}$ peak at 335.3 eV that corresponds to metallic Pd.[42] Upon sputtering, Dai and Davoli observed a new Pd $3d_{5/2}$ peak at 336.7 eV and a Si 2p peak at 99.5 eV ($+0.2$ eV shift from that of bulk Si), which they attributed to Pd_xSi at the interface.[42] In the present work, we could not see a clear indication of Pd_xSi formation from the Si 2p XPS peak, which remained nearly constant at 99.2 $\pm$ 0.1 eV with sputtering time, because of the overwhelming signal from bulk Si. For an oxidized Pd(110) surface, Peuckert assigned the Pd $3d_{5/2}$ peaks at 335.3 and 337.0 eV to metallic Pd and PdO, respectively,[43] and the strong intensity of the corresponding O 1s peak at 530.3 eV appeared to support the pres-

ence of PdO. In the present case, however, the intensity of the O 1s peak observed at 530.2 eV (discussed further below) is found to be too weak relative to that of the Pd $3d_{5/2}$, after appropriate correction by the respective sensitivity factor, to give the stoichiometry of PdO. The BE positions for the Pd $3d_{5/2}$ features for metallic Pd and Pd_xSi remain stable at 335.5 and 337.1 eV, respectively, with increasing sputtering time, and the corresponding BE difference (Pd − Pd_xSi) is effectively constant within the experimental uncertainty (±0.1 eV). The present work therefore provides the first clear evidence of the formation of Pd silicides, at room temperature, for Pd NPs electrodeposited on a Si surface.

In the Pd $3p_{3/2}$ and O 1s region (Figure 4, upper left), the as-deposited Pd NPs exhibit an intense O 1s peak at 533.0 eV corresponding to native Si oxides (SiO_x),[44] as expected from the oxidation of the H:Si surface not covered by nucleated Pd NPs in an aqueous solution during the electrodeposition process. Upon sputtering for 30 s, the O 1s peak has evidently become broadened and shifted to 532.0 eV. The O 1s BE shift is due to a change in the nature of the SiO_x species, as confirmed by the corresponding Si 2p feature that is found to shift from 102.7 to 101. eV (not shown). The strong O 1s feature of silicon oxides also obscures the weaker Pd $3p_{3/2}$ peak from metallic Pd at 532.6 eV. Further sputtering for

60 s broadens the spectral envelop further, which could be resolved into at least three components: two Pd $3p_{3/2}$ peaks at 532.6 and 533.7 eV for Pd and Pd_xSi, respectively, and one O 1s peak at 532.0 eV for SiO_x.[37] Evidently, there is insufficient intensity at 530.2 eV to identify PdO as a quantifiable component. Consistent with the Pd 3d spectral evolution (Figure 4, upper center), the Pd $3p_{3/2}$ peak at 532.6 eV for metallic Pd becomes the most prominent, while the Pd $3p_{3/2}$ for Pd_xSi and the O 1s feature for SiO_x are considerably weaker. With increasing sputtering time, the intensity of the Pd $3p_{3/2}$ peak at 533.7 eV for Pd_xSi becomes comparable to that of Pd $3p_{3/2}$ at 532.6 eV for metallic Pd, which has been similarly observed for the respective Pd 3d peaks for Pd_xSi and Pd (Figure 4, upper center). The Pd $3p_{1/2}$ region near 560 eV has also been carefully analyzed. Not surprisingly, similar intensity changes with sputtering have been found in the Pd $3p_{1/2}$ peaks at 560.0 and 561.3 eV, corresponding to metallic Pd and Pd_xSi, respectively.

For the VB spectra of sample A (Figure 4, upper right), the electron density of states (DOS) is found to be broadly distributed from 0 to 5 eV, with significant DOS at the Fermi level (E_F) characteristic of a metal. The as-deposited VB spectrum is in good accord with the spectrum of metallic Pd reported in the literature.[43,45] With increasing sputtering time, the DOS at the E_F (Supporting Information, Figure S5) appears to gradually shift to a higher BE, with the feature at ~3.5 eV becoming more notable. Given that the intensity changes for features at ~2.5 and ~3.5 eV with increasing sputtering time appear to vary in a similar fashion as those for Pd 3d and Pd 3p peaks for both Pd and Pd_xSi,[42] the features centered at 2.5 and 3.5 eV could be attributed to Pd and Pd_xSi. It should be noted that the peak at 9.2 eV corresponds to Ar 3p of implanted Ar, which increases in intensity with increasing sputtering time.

For the as-deposited Pd NPs on H:Si after annealing at 700 °C (sample A1), the Pd $3d_{5/2}$ (Pd $3d_{3/2}$) peak at 338.6 eV (344.0 eV) can be attributed to PdO_2 and/or hydrated PdO such as $Pd(OH)_4$,[37,46−48] with a measured spin−orbit splitting of 5.4 eV (Figure 4, lower center). Because PdO_2 is known to be unstable, it could also exist as a hydrous form, $Pd(OH)_2$.[49] Our assignment is consistent with those for Pd/SiO_2, obtained by reduction of Pd^{2+} ions over a SiO_2 support (in a solution) followed by calcination at 400 °C, for which Venezia et al. assigned the two Pd $3d_{5/2}$ peaks observed at 336.5 and 339.3 eV to PdO and PdO_2, respectively.[50] After 15 s of sputtering, the Pd 3d peaks become broadened (with the fwhm evidently increased from 1.3 to 2.2 eV for the Pd $3d_{5/2}$ peak), indicating the emergence of a new species at 336.7 eV. We assign this feature to PdO on the basis of a concomitant appearance of a new O 1s peak at 530.2 eV (to be discussed further below). The removal of the PdO_2 feature after a short sputtering suggests that the PdO_2 overlayer is rather thin, consistent with the lack of a sufficient scattering volume for detectable XRD signal. After 30 s of sputtering, the Pd $3d_{5/2}$ (Pd

$3d_{3/2}$) band can be easily resolved into two peaks at 335.3 eV (340.6 eV) and 336.7 eV (342.2 eV), attributed to metallic Pd and PdO, respectively. While the Pd $3d_{5/2}$ BE for the metallic Pd remains unchanged with sputtering time, the PdO feature appears to gradually shift to a higher BE (Figure 4, lower center). The fwhm of the peak at 337.0 eV BE (1.7 eV) for the annealed sample (Figure 4, lower center) is found to be broader than that for the unannealed Pd on H:Si (1.2 eV) (Figure 4 upper center), which suggests that the broader feature could contain, in addition to PdO, an additional component, likely Pd_xSi. To estimate the relative population of the PdO and Pd_xSi components, we use the area of the well-resolved O 1s peak at 530.2 eV for PdO to deduce the area of the Pd 3d component due to PdO (and correspondingly that of the Pd_xSi component), after appropriate consideration of the corresponding XPS relative sensitivity factors. For the spectrum after 30 s of sputtering, we estimated that 87% of the peak corresponds to PdO and 13% to Pd_xSi. After 60, 120, and 500 s of sputtering, the PdO relative population becomes 78, 45, and 26%, respectively. As expected with increasing sputtering time, the PdO component decreases while the Pd_xSi component increases as the XPS sampling volume approaches the Pd and Si interface. Consistent with the increase in Pd_xSi with increasing sputtering time, the maximum of the Pd $3d_{5/2}$ envelope also appears to shift to a higher BE due to the higher Pd 3d BE for Pd_xSi than that for PdO.[48] The PdO is sufficiently thick that the corresponding XRD pattern for the as-deposited sample A1 (Figure 3) reveals only PdO features without any Pd and Pd_xSi features. As an additional support for our present assignment, Otto et al. found for oxidized Pd supported on alumina[49] two Pd $3d_{5/2}$ peaks at 336.7 and 338.3 eV, which they assigned to PdO and PdO_2, respectively. They also observed a Pd $3d_{5/2}$ peak at 335.3 eV after sputter-cleaning, and one at 335.2 eV upon reduction in hydrogen condition, both of which they assigned to metallic Pd. Their results are in excellent agreement with our Pd peak positions and support our present assignments. Because we used the Si support, the additional peak at 337.0 (±0.1) eV found in the present work can be assigned to Pd_xSi.

The sputtering evolution of the Pd $3p_{3/2}$ and O 1s XPS features for sample A1 (Figure 4, lower left) is very similar to that found for sample A (Figure 4, upper left). The notably thicker SiO_x layer with characteristic O 1s feature at 533.2 eV is removed after sputtering for a longer time period (30 s). A better defined O 1s peak at 530.2 eV corresponding to PdO can be discerned after 15 s of sputtering and remains notable up to 500 s of sputtering, confirming the presence of the thicker PdO component in the annealed sample. The presence of a thick SiO_x layer is also supported by the Si 2p peak at 103.5 eV with increasing sputtering time (not shown).[51] The Pd $3p_{1/2}$ XPS peaks confirm the change in composition with sputtering time. For the as-prepared sample A1, a prominent Pd $3p_{1/2}$ peak is found at 563.5 eV, which we attribute to a PdO_2 overlayer.
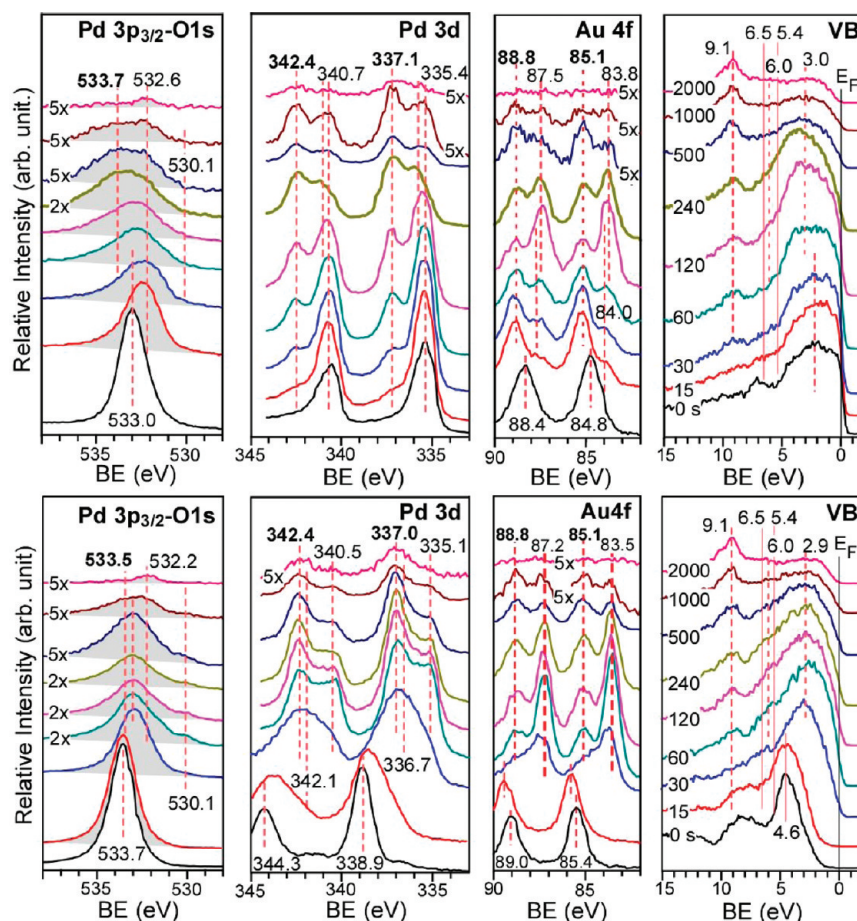
Figure 5. XPS spectra of the Pd 3p$_{3/2}$ and O 1s (far left), Pd 3d (center left), Au 4f (center right), and valence band (VB) regions (far right) for Pd NPs as-electrodeposited on a Au nanoisland template (sample B, upper) and after annealing at 700 °C for 1 h (sample B1, lower), and upon sputtering for 15, 30, 60, 120, 240, 500, 1000, and 2000 s.

The weaker, broad feature at 555 eV is likely due to a plasmon loss peak of Pd 3p$_{3/2}$ in PdO$_2$ (with no literature information reported), and its area (shaded area) appears to be reduced considerably upon 15 s of sputtering and completely removed after 30 s of sputtering, indicating complete removal of the PdO$_2$ component. Upon complete removal of PdO$_2$, the Pd 3p$_{1/2}$ peak becomes broader than that of sample A without postannealing, which indicates that the annealed sample (sample A1) contains more chemical species. Given that the Pd 3p$_{1/2}$ peak for sample A (without postannealing) can be resolved into the Pd$_x$Si and Pd components (Figure 4, upper left), the broader peak for sample A1, that is, with postannealing, (Figure 4, lower left) could therefore be due to the contribution from an additional PdO component.

Before sputtering begins, the VB spectrum of sample A1 (Figure 4, lower right) exhibits a well-defined peak at 4.2 eV, with negligible DOS (Supporting Information, Figure S5) at E_F consistent with the nonmetallic nature of the PdO$_2$ layer. After 15 s of sputtering, the VB spectrum becomes broadened and shifts to a lower BE (3.5 eV), with still a negligible DOS at E_F, indicating the absence of any metallic species. Upon 30 s of sputtering, the prominent VB feature has shifted to 2.3 eV, now with a significant DOS at E_F, which is consistent with

the emergence of the metallic Pd 3d$_{5/2}$ peak at 335.3 eV found after 30 s of sputtering (Figure 4, lower center). Further sputtering causes a spectral shift, broadening, and intensity reduction. The VB features for sample A1 after 30, 60, and 120 s of sputtering are found to be very similar to those taken for pressed bulk PdO powders and thin PdO films prepared *in situ*, reported by others.[52–54]

Figure 5 shows the XPS spectra of the Pd 3p$_{3/2}$ and O 1s, Pd 3d, Au 4f, and VB regions for Pd NPs electrodeposited on a Au NIT (sample B) and after annealing at 700 °C for 1 h (sample B1) over a range of sputtering time. Because the spectral evolution in Pd 3p and O 1s features with sputtering (Figure 5, upper far left) is similar to that found on the H:Si substrate (Figure 4, upper left), we will focus our discussion on the other three spectral regions. It should be noted that because the stronger Pd 3d$_{5/2}$ peak (at ~335.5 eV) occurs at the same BE as the Au 4d$_{5/2}$ peak,[36,37] we also carefully examined the less intense Pd 3d$_{3/2}$ peak (Figure 5, upper center left).[23] Evidently, for the as-deposited sample B, a prominent Pd 3d$_{5/2}$ (Pd 3d$_{3/2}$) peak at 335.4 eV (340.7 eV), attributed to metallic Pd, is clearly evident and consistent with our XRD result (Figure 3). Upon sputtering, the Pd 3d$_{5/2}$ peak at 337.1 eV due to Pd$_x$Si is found to in-

crease in intensity, with a concomitant decrease in the corresponding metallic Pd peak intensity.

The as-deposited sample B also exhibits an intense Au $4f_{7/2}$ (Au $4f_{5/2}$) peak at 84.8 eV (88.4 eV) with a fwhm of 1.5 eV (Figure 5, upper center right). Located at 0.8 eV higher in BE than that of metallic Au but only 0.3 eV lower than that of Au silicide,[33] this broad feature is likely a mixture of both metallic Au and Au silicide. After 15 s of sputtering occurs, this feature evolves into two sharper Au $4f_{7/2}$ features at 83.8 and 85.1 eV, with respective fwhms of 1.0 and 1.2 eV, which can be assigned to metallic Au and Au silicide, respectively.[33] The BE positions of the two peaks remain effectively unchanged with increasing sputtering time. The presence of Au silicide is due to desorption of the Au nanoislands during the electrodeposition process, which exposes the Au silicide interfacial region (Supporting Information, Figure S6). We found no indication of Pd deposition onto the exposed Au silicide locations during subsequent electrodeposition. More details regarding field-induced desorption of Au nanoislands are given elsewhere.[55] The "metallic" Au $4f_{7/2}$ feature at 83.8 eV is discernibly lower by 0.2 eV than that of metallic Au NPs on Si(100),[33] which could indicate a Pd−Au alloying effect, in accord with the notable XRD shifts observed in the Au(111) feature from 38.3° for Au NIT to 38.5° for Pd/Au by +0.2° and in the Pd(111) feature from 40.2_3° for Pd to 40.1_9° for Pd−Au by -0.04° (Figure 3). This might be the first clear XRD evidence for the formation of Pd−Au alloy by electrodeposition.[56] Further sputtering to 120 s has produced the strongest metallic Au $4f_{7/2}$ feature at 83.8 eV. Above 120 s and to 500 s of sputtering, the intensity of the metallic Au $4f_{7/2}$ feature appears to become reduced considerably while the intensity of the corresponding Au silicide $4f_{7/2}$ feature is depleted at a slower rate, as the Au nanoislands are being removed.

The VB spectra for the as-deposited sample B and upon sputtering (Figure 5, upper far right) are generally similar to those of sample A (Figure 4, upper right). In particular, the abrupt DOS at the Fermi edge, with the majority of the DOS located at 0.5−4 eV, clearly indicates the metallic nature of the sample.[43,45] A notable difference between the VB spectra of the two samples is the enhanced intensity near 6.0 eV for sample B, which is due to the contributions of Au and Au silicide. Detailed discussion of similar VB signature for Au and Au silicide has been given in our earlier work.[33]

For Pd NPs electrodeposited on Au NIT after annealing at 700 °C for 1 h (sample B1), significant changes to the Pd 3d region and especially the O 1s signal at 530.1 eV (in the Pd $3d_{5/2}$−O1s region, which resembles that of sample A1 in Figure 4 lower, discussed earlier) are observed, with the corresponding spectral evolution with increasing sputtering time (Figure 5, lower center left) resembling those of Pd NPs on H:Si after annealing (sample A1, Figure 4, lower left). In particular, a sharp Pd $3d_{5/2}$ (Pd $3d_{3/2}$) peak at 338.9 eV (344.3 eV), corresponding to PdO_2, is clearly observed for the as-

prepared sample B1, and upon 15 s of sputtering, it becomes broader due to contribution from the Pd $3d_{5/2}$ (Pd $3d_{2/2}$) peak at 336.7−337.0 eV (342.1−342.4 eV) for PdO[43,49] (as discussed above for sample A1). Further sputtering to 30 s totally removes the PdO_2 features and sharpens the PdO features while exposing a new Pd $3d_{5/2}$ (Pd $3d_{3/2}$) peak at 335.1 eV (340.5 eV) corresponding to metallic Pd.[42,43] The Pd 3d spectrum, after sputtering sample B1 for 60 s, clearly exhibits two chemical components corresponding to metallic Pd and PdO. However, like the spectra of Pd NPs on H:Si in Figure 4 (upper center), we should also consider the possible presence of Pd_xSi features near 337.0 eV. In addition, upon curve-fitting with two peaks, the higher-BE Pd $3d_{5/2}$ peak at 336.7−337.0 eV exhibits a much broader fwhm (1.7 eV) than that for sample B without postannealing (1.3 eV). The larger width suggests that the feature at the higher BE could contain a Pd_xSi component, in addition to the PdO component. We estimated the relative composition of Pd_xSi to PdO to be 3:7 for sample B1 after 60 s of sputtering. This Pd_xSi to PdO ratio is found to gradually increase with increasing sputtering time, consistent with the expected increase in the Pd_xSi as the sampling volume approaches the Au nanoisland interface.

For the as-prepared sample B1, the corresponding Au $4f_{7/2}$ (Au $4f_{5/2}$) peak is initially seen at 85.4 eV (89.0 eV), with a fwhm of 1.1 eV (Figure 5, lower center right). A short 15 s of sputtering appears to shift the Au $4f_{7/2}$ peak to a higher BE (85.7 eV) with a broader fwhm (1.3 eV). Upon further sputtering to 30 s, the Au $4f_{7/2}$ XPS peak is clearly resolved into two peaks at 83.5 and 85.1 eV, with respective fwhms of 0.9 and 1.4 eV. Like sample B without postannealing, the Au silicide feature at 85.1 eV for sample B1 shows no discernible change in BE position upon further sputtering. As we propose for sample B, the observation of Au silicide related XPS features is due to field-induced desorption of the Au nanoislands, which causes exposure of the Au silicide interfacial region.[55] These areas are not expected to affect the formation of Pd NPs on the remaining (undesorbed) Au nanoislands. However, the stronger Au $4f_{7/2}$ peak at 83.5 eV has evidently shifted to a lower BE by 0.5 eV than metallic Au[33] upon thermal annealing (Figure 5, lower center right). The considerable BE shift is clear evidence for the formation of Pd−Au alloy, in good accord with the Pd 3d XPS (Figure 5, lower center left) and XRD data (Figure 3) observed above. For five monolayers of Pd vapor-deposited on five monolayers of Au supported on Mo(110) in ultrahigh vacuum condition, Yi et al. observed BE shifts of ~0.45 and 0.15 eV to a lower BE for Au $4f_{7/2}$ and Pd $3d_{3/2}$ peaks, respectively, after annealing at 800 °C, and they attributed these BE shifts as evidence for the formation of Pd−Au alloys.[24] Moreover, the present Au 4f spectra (Figure 5, lower center right) are in very good agreement with the other Pd−Au alloys prepared under different conditions.[16,57,58] For the Au $4f_{7/2}$ XPS peaks at 85.4 and 84.8 eV for the as-prepared samples B1 and B (before
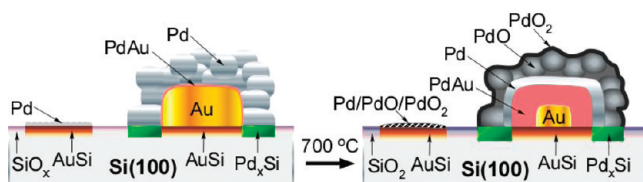
Figure 6. Simplified diagram showing the main compositions of Pd nanodeposits on a Au nanoisland before and after annealing at 700 °C. Pd, PdO, and PdO_2 are plausible Pd components in the AuSi region upon thermal annealing.

sputtering), respectively (Figure 5), it is unclear if the BE shift (from metallic Au) is due to that exposed Au silicide and/or some other Au complexes as a result of a high-temperature reaction with CO_2 (or CO), H_2O, and O_2.[59] For these Au features, we could rule out the formation of Au oxides due to the lack of the O 1s peak near 530.0 eV corresponding to AuO_x[60,61] for the as-prepared sample B1 and with 15 s of sputtering. The VB spectra for sample B1 (Figure 5, lower far right) are found to be generally similar to those for sample A1 (Figure 4, lower right) over the sputtering depth. Owing to the contribution from Au (at 3.0 and 6.0 eV) and Au silicide (at 5.4 and 6.5 eV), the VB spectral features for sample B1 appear to be located at higher BEs with larger widths than those for sample A1, with for example, the band maxima found at 3.7 and 2.9 eV for the as-prepared sample B1 and after 30 s of sputtering, respectively.

On the basis of our experimental data, we present a simplified diagram in Figure 6 to summarize the discernible compositions of Pd nanodeposits on Au nanoislands before and after the 700 °C postannealing. For the as-deposited Pd NPs on Au NIT (Figure 6, left), metallic Pd is the major component, with PdAu and Pd_xSi found at the respective interfaces of Au nanoislands and the Si substrate. As shown in our recent work,[33] the formation of AuSi has been confirmed at the interface between the Au nanoislands and the Si substrate. Upon being annealed at 700 °C in air for 1 h, the metallic Pd region becomes depleted with the conversion to PdAu alloy at the Au interface and with the formation of PdO covered by a thin PdO_2 overlayer at the air side. The observation of AuSi XPS features at the early stage of sputtering can be explained by field-induced desorption of Au nanoislands during the subsequent electrodeposition of Pd. The exposed AuSi areas are covered by Pd, which becomes mixed oxide composites.

CONCLUSIONS

Palladium was electrodeposited directly on a H-terminated Si(100) substrate and on a Au NIT sup-

ported on Si(100). The morphology and crystal structures, as well as the electronic structures and chemical-state composition of the as-deposited and postannealed samples were studied in detail by using SEM/EDX, GIXRD, and depth-profiling XPS. Depth-profiling XPS experiments show that the jagged cuboid as-deposited Pd NPs on H:Si consist primarily of a metallic Pd core with Pd_xSi formed at the Pd and Si interface. Annealing the Pd NPs to 700 °C in air promotes the formation of PdO with an overlayer of PdO_2. In the case of Pd NPs electrodeposited on a supported Au NIT, we observe the formation of PdAu alloy for the first time at room temperature at the metallic Pd and Au nanoisland interface. The PdAu alloy formation can be further enhanced by postannealing at 700 °C in air and is definitively identified by the shifts of the Pd $3d_{3/2}$ and the metallic Au $4f_{7/2}$ features to lower BEs, and further confirmed by the convergence of the respective XRD Pd and Au features to common, intermediate 2θ positions. The lack of discernible change in the Au $4f_{7/2}$ peak position at 85.1 eV indicates that the inner Au silicide is not critically impacted by Pd electrodeposition (on the perimeter of the Au nanoislands) and thermal annealing. The SEM images and the corresponding EDX analysis further reveal that the Pd nanodeposit on a Au nanoisland in the annealed sample appears "smooth" without the presence of jagged cuboid nanostructures and it consists of Au-rich, Pd-rich, and comparable Au−Pd mixed regions. These different regions are expected to show different catalytic activities. It may also be quite feasible to tune the exposed surface, for example, Pd or PdAu alloy, selectively for appropriate catalytic reactions by further processing of these as-prepared hybrid nanomaterials. These core−shell structures could also be potentially applied to sensing and surface-enhanced Raman scattering (SERS).[62−64] The sensing and SERS signals could be controlled and enhanced by manipulating the core−shell structures. Our work also demonstrates that by using Au nanoisland templates, it is possible to easily prepare other bimetallic nanosystems with a transition metal-shell and a Au-core, such as Cu/Au, Ni/Au, and Fe/Au. To illustrate the growth process of Pd on the Au nanoislands, we have chosen the size of the nanoislands to be about 100 nm. However, this size can be reduced substantially as shown in our recent work,[33] and the synthesis of these bimetallic nanosystems over an extended size range (e.g., down to 10 nm) can be easily achieved, which may in turn offer further flexibility in controlling the reactivity and selectivity of specific chemical processes.

EXPERIMENTAL DETAILS

The Au NIT was prepared on a Si(100) substrate using a method discussed in detail in our recent work.[33] Briefly, Au was deposited on a Si(100) substrate by magnetron sputtering in an argon atmosphere in a Denton Desk II magnetron sputter-coater. The Au nanofilm was then annealed in air in a conventional

oven to produce near-regularly spaced nanoislands with a well-defined, reproducible size distribution.[33] This postannealing step also introduced (nonconducting) thermal oxide in an area not covered by the Au nanoislands on the Si support, thereby restricting NP growth only on the Au nanoislands for the subsequent Pd electrodeposition. In the case when the thickness of

the oxide layer was too thick, we could achieve more efficient Pd deposition by reducing the oxide thickness by dipping in 1% HF solution for less than 30 s. The Si(100) substrate, 2.5 × 15 mm² in size, was cut from a single-side-polished p-type (B-doped) Si(100) wafer (0.4 mm thick, purchased from Waferworld), with a resistivity of $1.0-1.5$ mΩ cm. Detailed characterization of the resulting Au NIT and the control of its spatial configuration (with specific average size distribution and number density) have also been given in our recent work.[33]

Electrochemical deposition of Pd on the supported Au NIT (serving as the working electrode) was carried out in a three-electrode cell (with a Ag/AgCl reference and Pt wire counter electrodes) using a CH Instruments 660A electrochemical workstation. For comparison with the Au NIT supported on a Si(100) substrate, a Si(100) substrate hydrogen-terminated by pretreatment in a 1% HF solution has also been used as the working electrode for the Pd deposition. A solution of 1 mM $PdSO_4$ (98% purity, Aldrich) and 30 mM HCl was used as the electrolyte. After the Pd electrodeposition, the sample was thoroughly rinsed with Millipore water (18.2 MΩ cm resistivity), and was dried in a N_2 environment before the characterization experiments. The as-prepared Pd and Pd/Au samples were annealed at 700 °C for 1 h in air under ambient condition.

A LEO 1530 field-emission scanning electron microscope was used for SEM morphology study and EDX analysis of the Pd nanodeposits on a Au NIT. The corresponding crystal structures of the Pd−Au NIT system were determined by GIXRD in a PANalytical X'Pert Pro MRD diffractometer, with the Cu Kα anode operating at 45 kV and 40 mA and positioned at an incident angle of 0.6°. The chemical states of the samples were analyzed as a function of Ar^+ sputtering time (depth) by XPS by using a Thermo-VG Scientific ESCALab 250 microprobe, with a monochromatic Al Kα X-ray source (1486.6 eV) at a typical energy resolution of $0.4-0.5$ eV full width at half-maximum (fwhm). An Ar^+ ion beam with 3 keV beam energy was used to deliver an ion current density of $0.3-0.4$ μA mm⁻² on the sample during sputtering.

Supporting Information Available: Cyclic voltammetry curve for Pd deposition on Au NIT supported on Si; additional EDX and XPS spectra; SEM image showing desorption of a number of Au NPs during Pd deposition on Au NIT supported on Si. This material is available free of charge *via* the Internet at http://pubs.acs.org.

REFERENCES AND NOTES

1. Han, Y.-F.; Kumar, D.; Sivadinarayana, C.; Goodman, D. W. Kinetics of Ethylene Combustion in the Synthesis of Vinyl Acetate over a Pd/SiO₂ Catalyst. *J. Catal.* **2004**, *224*, 60–68.
2. Pallassana, V.; Neurock, M. Electronic Factors Governing Ethylene Hydrogenation and Dehydrogenation Activity of Pseudomorphic Pd_{ML}/Re(0001), Pd_{ML}/Ru(0001), Pd(111), and Pd_{ML}/Au(111) Surfaces. *J. Catal.* **2000**, *191*, 301–317.
3. Piednoir, A.; Languille, M. A.; Piccolo, L.; Valcarcel, A.; Cadete Santos Aires, F. J.; Bertolini, J. C. Pd(111) *versus* Pd-Au(111) in Carbon Monoxide Oxidation under Elevated Pressures. *Catal. Lett.* **2007**, *114*, 110–114.
4. Enache, D. I.; Edwards, J. K.; Landon, P.; Solsona-Espriu, B.; Carley, A. F.; Herzing, A. A.; Watanabe, M.; Kiely, C. J.; Knight, D. W.; Hutchings, G. J. Solvent-Free Oxidation of Primary Alcohols to Aldehydes Using Au-Pd/TiO₂ Catalysts. *Science* **2006**, *311*, 362–365.
5. Narayanan, R.; El-Sayed, M. A. Catalysis with Transition Metal Nanoparticles in Colloidal Solution: Nanoparticle Shape Dependence and Stability. *J. Phys. Chem. B* **2005**, *109*, 12663–12676.
6. Mazzone, G.; Rivalta, I.; Russo, N.; Sicilia, E. Interaction of CO with PdAu(111) and PdAu(100) Bimetallic Surfaces: A Theoretical Cluster Model Study. *J. Phys. Chem. C* **2008**, *112*, 6073–6081.
7. Scott, R. W. J.; Sivadinarayana, C.; Wilson, O. M.; Yan, Z.; Goodman, D. W.; Crooks, R. M. Titania-Supported PdAu Bimetallic Catalysts Prepared from Dendrimer-Encapsulated Nanoparticle Precursors. *J. Am. Chem. Soc.* **2005**, *127*, 1380–1381.
8. Chen, M.; Kumar, D.; Yi, C.-W.; Goodman, D. W. The Promotional Effect of Gold in Catalysis by Palladium−Gold. *Science* **2005**, *310*, 291–293.
9. García-Mota, M.; Loìpez, N. Template Effects in Vinyl Acetate Synthesis on PdAu Surface Alloys: A Density Functional Theory Study. *J. Am. Chem. Soc.* **2008**, *130*, 14406–14407.
10. Yuan, D.; Gong, X.; Wu, R. Origin of High Activity and Selectivity of PdAu(001) Bimetallic Surfaces toward Vinyl Acetate Synthesis. *J. Phys. Chem. C* **2008**, *112*, 1539–1543.
11. Ogihara, H.; Takenaka, S.; Yamanaka, I.; Tanabe, E.; Genseki, A.; Otsuka, K. Formation of Highly Concentrated Hydrogen Through Methane Decomposition over Pd-Based Alloy Catalysts. *J. Catal.* **2006**, *238*, 353–360.
12. Sarkany, A. Semi-hydrogenation of 1,3-Butadiene on Adspecies Modified Pd−Ni, Co, and Cu Catalysts. *Appl. Catal., A* **1997**, *149*, 207–223.
13. Wei, T.; Wang, J.; Goodman, D. W. Characterization and Chemical Properties of Pd−Au Alloy Surfaces. *J. Phys. Chem. C* **2007**, *111*, 8781–8788.
14. Landon, P.; Collier, P. J.; Papworth, A. J.; Kiely, C. J.; Hutchings, G. J. Direct Formation of Hydrogen Peroxide from H₂/O₂ Using a Gold Catalyst. *Chem. Commun.* **2002**, *18*, 2058–2059.
15. Solsona, B. E.; Edwards, J. K; Landon, P.; Carley, A. F.; Herzing, A.; Kiely, C. J.; Hutchings, G. J. Direct Synthesis of Hydrogen Peroxide from H₂ and O₂ Using Al₂O₃ Supported Au−Pd Catalysts. *Chem. Mater.* **2006**, *18*, 2689–2695.
16. Han, Y.-F.; Zhong, Z.; Ramesh, K.; Chen, F.; Chen, L.; White, T.; Tay, Q.; Yaakub, S. N.; Wang, Z. Au Promotional Effects on the Synthesis of H₂O₂ Directly from H₂ and O₂ on Supported Pd−Au Alloy Catalysts. *J. Phys. Chem. C* **2007**, *111*, 8410–8413.
17. Lee, A. F.; Baddeley, C. J.; Hardacre, C.; Ormerod, R. M.; Lambert, R. M.; Schmid, G.; West, H. Structural and Catalytic Properties of Novel Au/Pd Bimetallic Colloid Particles: EXAFS, XRD, and Acetylene Coupling. *J. Phys. Chem.* **1995**, *99*, 6096–6102.
18. Baddeley, C. J.; Ormerod, R. M.; Stephenson, A. W.; Lambert, R. M. Surface Structure and Reactivity in the Cyclization of Acetylene to Benzene with Pd Overlayers and Pd/Au Surface Alloys on Au{111}. *J. Phys. Chem.* **1995**, *99*, 5146–5151.
19. Piccolo, L.; Piednoir, A.; Bertolini, J. -C. Pd−Au Single-Crystal Surfaces: Segregation Properties and Catalytic Activity in the Selective Hydrogenation of 1,3-Butadiene. *Surf. Sci.* **2005**, *592*, 169–181.
20. Villa, A.; Campione, C.; Prati, L. Bimetallic Gold/Palladium Catalysts for the Selective Liquid Phase Oxidation of Glycerol. *Catal. Lett.* **2007**, *115*, 133–136.
21. Juszczyk, W.; Karpinski, Z.; Lomot, D.; Pielaszek, J.; Sobczak, J. W. Pd-Au/SiO₂: Characterization and Catalytic Activity. *J. Catal.* **1995**, *151*, 67–76.
22. Ferri, D.; Behzadi, B.; Kappenberger, P.; Hauert, R.; Ernst, K. -H.; Baiker, A. Probing the Interface in Vapor-Deposited Bimetallic Pd−Au and Pt−Au Films by CO Adsorption from the Liquid Phase. *Langmuir* **2007**, *23*, 1203–1208.
23. Xiang, Y.; Wu, X.; Liu, D.; Jiang, X.; Chu, W.; Li, Z.; Ma, Y.; Zhou, W.; Xie, S. Formation of Rectangularly Shaped Pd/Au Bimetallic Nanorods: Evidence for Competing Growth of the Pd Shell between the {110} and {100} Side Facets of Au Nanorods. *Nano Lett.* **2006**, *6*, 2290–2294.
24. Yi, C. -W.; Luo, K.; Wei, T.; Goodman, D. W. The Composition and Structure of Pd−Au Surfaces. *J. Phys. Chem. B* **2005**, *109*, 18535–18540.
25. Shen, X.; Frankel, D. J.; Hermanson, J. C.; Lapeyre, G. J.; Smith, R. J. Photoemission Studies of Ordered Pd Overlayers on Au(111): Implications for CO Chemisorption. *Phys. Rev. B* **1985**, *32*, 2120–2125.

26. Toshima, N.; Yonezawa, T. Bimetallic Nanoparticles—Novel Materials for Chemical and Physical Applications. *New J. Chem.* **1998**, *22*, 1179–1201.

27. Dash, P.; Bond, T.; Fowler, C.; Hou, W.; Coombs, N.; Scott, R. W. J. Rational Design of Supported PdAu Nanoparticle Catalysts from Structured Nanoparticle Precursors. *J. Phys. Chem. C* **2009**, *113*, 12719–12730.

28. Maroun, F.; Ozanam, F.; Magnussen, O. M.; Behm, R. J. The Role of Atomic Ensembles in the Reactivity of Bimetallic Electrocatalysts. *Science* **2001**, *293*, 1811–1814.

29. Naohara, H.; Ye, S.; Uosaki, K. Electrochemical Layer-by-Layer Growth of Palladium on an Au(111) Electrode Surface: Evidence for Important Role of Adsorbed Pd Complex. *J. Phys. Chem. B* **1998**, *102*, 4366–4373.

30. Kibler, L. A.; Kleinert, M.; Randler, R.; Kolb, D. M. Initial Stages of Pd Deposition on Au(*hkl*) Part I: Pd on Au(111). *Surf. Sci.* **1999**, *443*, 19–30.

31. Stafford, G. R.; Bertocci, U. *In Situ* Stress and Nanogravimetric Measurements During Underpotential Deposition of Pd on (111)-Textured Au. *J. Phys. Chem. C* **2009**, *113*, 261–268.

32. Baldauf, M.; Kolb, D. M. Formic Acid Oxidation on Ultrathin Pd Films on Au(*hkl*) and Pt(*hkl*) Electrodes. *J. Phys. Chem.* **1996**, *100*, 11375–11381.

33. Sohn, Y.; Pradhan, D.; Radi, A.; Leung, K. T. Interfacial Electronic Structure of Gold Nanoparticles on Si(100): Alloying *versus* Quantum Size Effects. *Langmuir* **2009**, *25*, 9557–9563.

34. *PDF-2 Database*; International Center for Diffraction Data: Newtown Square, PA, 2004.

35. Abdelsayed, V.; Saoud, K, M.; Samy El-Shall, M. Vapor Phase Synthesis and Characterization of Bimetallic Alloy and Supported Nanoparticle Catalysts. *J. Nanoparticle Res* **2006**, *8*, 519–531.

36. Moulder, J. F.; Stickle, W. F.; Sobol, P. E.; Bomben, K. D. *Handbook of X-ray Photoelectron Spectroscopy,* 2nd ed.; Chastain, J., Ed.; Perkin-Elmer Corp.: Eden-Prairie, MN, 1992.

37. *NIST X-ray Photoelectron Spectroscopy Database,* version 3.5; National Institute of Standards and Technology: Gaithersburg, 2003; http://srdata.nist.gov/xps/.

38. Hara, S.; Yoshimura, M.; Ueda, K. Pd adsorption on Si(113) Surface: STM and XPS Study. *Appl. Surf. Sci.* **2008**, *254*, 7797–7802.

39. Okado, H.; Sakata, T.; Ukezono, Y.; Hirono, S.; Mori, H. Room Temperature Formation of Crystallized Palladium Silicide on Si(111) Observed by Ultrahigh Voltage Electron Microscopy. *Jpn. J. Appl. Phys.* **2002**, *41*, L344–L346.

40. Rubloff, G. W.; Ho, P. S.; Freeouf, J. F.; Lewis, J. E. Chemical Bonding and Reactions at the Pd/Si Interface. *Phys. Rev. B* **1981**, *23*, 4183–4196.

41. Ye, X. R.; Wai, C. M.; Zhang, D.; Kranov, Y.; McIlroy, D. N.; Lin, Y.; Engelhard, M. Immersion Deposition of Metal Films on Silicon and Germanium Substrates in Supercritical Carbon Dioxide. *Chem. Mater.* **2003**, *15*, 83–91.

42. Dai, D. -X.; Davoli, I. An Experimental Study of an Interface Reaction at the Practical Pd/Si Interface by XPS. *Vacuum* **1995**, *46*, 139–142.

43. Peuckert, M. XPS Study on Surface and Bulk Palladium Oxide, Its Thermal Stability, and a Comparison with Other Noble Metal Oxides. *J. Phys. Chem.* **1985**, *89*, 2481–2486.

44. Amy, F.; Soukiassian, P.; Hwu, Y. K.; Brylinski, C. Si-rich 6*H*- and 4*H*-SiC(0001) 3 × 3 Surface Oxidation and Initial SiO₂/SiC Interface Formation from 25 to 650 °C. *Phys. Rev. B* **2002**, *65*, 165323/1–165323/11.

45. Weissman-Wenocur, D. L.; Stefan, P. M.; Pate, B. B.; Shek, M. L.; Lindau, I.; Spicer, W. E. Photoemission Study of Au Overlayers on Pd(111) and the Formation of a Pd—Au(111) Alloy Surface. *Phys. Rev. B* **1983**, *27*, 3308–3317.

46. Barr, T. L. An ESCA Study of the Termination of the Passivation of Elemental Metals. *J. Phys. Chem.* **1978**, *82*, 1801–1810.

47. Kim, K. S.; Gossmann, A. F.; Winograd, N. X-ray Photoelectron Spectroscopic Studies of Palladium Oxides and the Palladium—Oxygen Electrode. *Anal. Chem.* **1974**, *46*, 197–200.

48. Briggs, D.; Seah, M.-P. *Practical Surface Analysis*, 2nd ed.; John Wiley & Sons: New York, 1993; Vol. 1.

49. Otto, K.; Haack, L. P.; deVries, J. E. Identification of Two Types of Oxidized Palladium on γ-Alumina by X-ray Photoelectron Spectroscopy. *Appl. Catal., B* **1992**, *1*, 1–12.

50. Venezia, A. M.; Liotta, L. F.; Pantaleo, G.; La Parola, V.; Deganello, G.; Beck, A.; Koppany, Z.; Frey, K.; Horvath, D.; Guczi, L. Activity of SiO₂ Supported Gold—Palladium Catalysts in CO Oxidation. *Appl. Catal., A* **2003**, *251*, 359–368.

51. Ulgut, B.; Suzer, S. XPS Studies of SiO₂/Si System under External Bias. *J. Phys. Chem. B* **2003**, *107*, 2939–2943.

52. Pillo, Th.; Zimmermann, R.; Steiner, P.; Hufner, S. The Electronic Structure of PdO Found by Photoemission (UPS and XPS) and Inverse Photoemission (BIS). *J. Phys.: Condens. Matter* **1997**, *9*, 3987–3999.

53. Brun, M.; Berthet, A.; Bertolini, J. C. XPS, AES, and Auger Parameter of Pd and PdO. *J. Electron Spectrosc. Relat. Phenom.* **1999**, *104*, 55–60.

54. Holl, Y.; Krill, G.; Amamou, A.; Legare, P.; Hilaire, L; Maire, G. Electronic Structure of PdO Studied by Photoemission XPS, UPS. *Solid State Commun.* **1979**, *32*, 1189–1192.

55. Sohn, Y.; Pradhan, D.; Leung, K. T., in preparation.

56. Pinheiro, A. L. N.; Zei, M. S.; Luo, M. F.; Ertl, G. The Epitaxial Growth of Pd Electrodeposition on Au(100) Studied by LEED and RHEED. *Surf. Sci.* **2006**, *600*, 641–650, and references cited therein.

57. Lee, Y.-S.; Jeon, Y.; Chung, Y.-D.; Lim, K.-Y.; Whang, C.-N.; Oh, S.-J. Charge Redistribution and Electronic Behavior in Pd—Au Alloys. *J. Korean Phys. Soc.* **2000**, *37*, 451–455.

58. Nascente, P. A. P.; de Castro, S. G. C.; Landers, R.; Kleiman, G. G. X-ray Photoemission and Auger Energy Shifts in Some Gold-palladium Alloys. *Phys. Rev. B* **1991**, *43*, 4659–4666.

59. Stephen, A.; Hashmi, K.; Hutchings, G. J. Gold Catalysis. *Angew. Chem., Int. Ed.* **2006**, *45*, 7896–7936.

60. Juodkazis, K.; Juodkazyte, J.; Jasulaitiene, V.; Lukinskas, A.; Sebeka, B. XPS Studies on the Gold Oxide Surface Layer Formation. *Electrochem. Commun.* **2000**, *2*, 503–507.

61. Torres, J.; Perry, C. C.; Bransfield, S. J.; Fairbrother, D. H. Radical Reactions with Organic Thin Films: Chemical Interaction of Atomic Oxygen with an X-ray Modified Self-Assembled Monolayer. *J. Phys. Chem. B* **2002**, *106*, 6265–6272.

62. Lee, Y. W.; Kim, N. H.; Lee, K. Y.; Kwon, K.; Kim, M; Han, S. W. Synthesis and Characterization of Flower-Shaped Porous Au—Pd Alloy Nanoparticles. *J. Phys. Chem. C* **2008**, *112*, 6717–6722.

63. Zhang, K.; Xiang, Y.; Wu, X.; Feng, L.; He, W.; Liu, J.; Zhou, W.; Xie, S. Enhanced Optical Responses of Au@Pd Core/Shell Nanobars. *Langmuir* **2009**, *25*, 1162–1168.

64. Beeram, S. R.; Zamborini, F. P. Selective Attachment of Antibodies to the Edge Sites of Gold Nanostructures for Enhanced Localized Surface Plasmon Resonance Biosensing. *J. Am. Chem. Soc.* **2009**, *131*, 11689–11691.